

Epitaxial and Fiber-Textured Stacks of $\text{Al}_{0.7}\text{Sc}_{0.3}\text{N}/\text{Mo}/\text{AlN}$ Prepared by Magnetron Sputter Epitaxy for Bulk Acoustic Wave Devices: A Comparison using High Overtone Bulk Acoustic Wave Resonator

Balasubramanian Sundarapandian,* Niclas M. Feil, Lutz Kirste, Patrik Straňák, Mario Prescher, Mohit Raghuwanshi, and Oliver Ambacher

Emerging 5G telecommunication has increased the demand for filters with high performance and wide bandwidth. Aluminum scandium nitride (AlScN) bulk acoustic wave resonators offer high quality factor (Q) and effective electromechanical coupling coefficient (k_{eff}^2), making them a promising candidate for 5G filters, due to their high piezoelectric coefficient (d_{33}) and intrinsic electromechanical coupling coefficient (k_t^2). This study compares high overtone bulk acoustic wave resonators (HBAR) fabricated using fiber textured and epitaxial stacks of aluminum nitride (AlN), molybdenum (Mo), and AlScN on silicon (Si) substrates prepared by magnetron sputtering. The mosaicity, crystal texture, thickness, and piezoelectric properties of the sputtered films are studied using X-ray diffraction (XRD), time-of-flight secondary ion mass spectrometry, and Berlincourt piezometry. Additionally, the frequency response of the resonators is studied using a vector network analyzer. The comparison revealed that the HBAR fabricated using epitaxial stack of AlScN/Mo/AlN/Si have a higher k_{eff}^2 and Q than the fiber-textured stack. Consequently, the figure of merit ($k_{\text{eff}}^2 \times Q$) calculated at ≈ 4 GHz indicates a 25% improvement in resonator performance. The study also shows that epi-AlScN (XRD AlScN 0002 ω -full width at half maximum (FWHM) = 1.91°) grown on epitaxial Mo (XRD Mo 110 ω -FWHM = 0.63°) has superior crystalline quality than its fiber-textured equivalent.

1. Introduction


The emerging 5G telecommunication standards require wide bandwidth filters for operation at frequencies ranging between 3.3 and 5.9 GHz while minimizing acoustic loss.^[1] Bulk acoustic wave (BAW) resonators exhibiting a high electro-mechanical coupling coefficient (k_{eff}^2), high quality factor (Q), and low temperature coefficient of frequency (TCF) have become the go-to choice to meet the requirements imposed by the telecommunication industry.^[2–5] Aluminum nitride (AlN) thin films, with intrinsic electromechanical coupling coefficient $k_t^2 = 6.5\%$ ^[6] and piezoelectric coefficient $d_{33} = 6 \text{ pC N}^{-1}$,^[7] are state of the art owing to their ease of being integrated in a semiconductor fab environment. Akiyama et al. have shown that by alloying AlN with scandium nitride (ScN), the piezoelectric response can be increased by 400%.^[8] Aluminum scandium nitride ($\text{AlAl}_{1-x}\text{Sc}_x\text{N}$ or AlScN) can provide relatively high k_t^2 and d_{33} , while maintaining decent Q values. $\text{Al}_{0.7}\text{Sc}_{0.3}\text{N}$ was found

to have k_t^2 of 15% and a longitudinal piezoelectric response of 16 pC N^{-1} ,^[8,9] making it a compelling choice for BAW resonators. Single-crystal epitaxial AlN-based film acoustic bulk acoustic wave resonator (FBAR) technology was found to have a k_{eff}^2 double that of polycrystalline AlN.^[10] Vetry et al. showed that the power handling capabilities of single crystal AlN are superior to a fiber-textured AlN.^[11] Loebl et al. have shown that the k_{eff}^2 improves with the c -axis orientation of the AlN grains.^[12] Epitaxial AlScN is expected to follow the same trend and, therefore, is a desirable material choice for BAW resonators.

In addition to the piezoelectric material, the choice of electrode is also crucial for determining the BAW resonator properties. An optimum electrode material for FBAR should have high acoustic impedance (z_{ac}), low resistivity, and low mass density ρ . A large difference in z_{ac} between piezoelectric and electrode material is desired to confine acoustic waves in the piezoelectric material and thereby improve the k_{eff}^2 of the resonators.

B. Sundarapandian, L. Kirste, P. Straňák, M. Prescher, M. Raghuwanshi
Department of Epitaxy
Fraunhofer Institute for Applied Solid State Physics
Tullastraße 72, 79108 Freiburg im Breisgau, Germany
E-mail: balasubramanian.sundarapandian@iaf.fraunhofer.de

N. M. Feil, O. Ambacher
Institute for Sustainable Systems Engineering (INATECH)
University of Freiburg
79110 Freiburg im Breisgau, Germany

 The ORCID identification number(s) for the author(s) of this article can be found under <https://doi.org/10.1002/pssa.202500189>.

© 2025 The Author(s). physica status solidi (a) applications and materials science published by Wiley-VCH GmbH. This is an open access article under the terms of the Creative Commons Attribution License, which permits use, distribution and reproduction in any medium, provided the original work is properly cited.

DOI: 10.1002/pssa.202500189

Low resistivity is particularly crucial for improving Q , while low mass density helps reduce mass loading. Previous studies have shown that Mo-based solidly mounted resonator and FBAR have low acoustic losses^[13] and better performance^[14] when compared to metals like titanium (Ti), copper (Cu), gold (Au), chromium (Cr), aluminum (Al), ruthenium (Ru), and tungsten (W). Therefore, Mo was used as the bottom electrode in this work. In our previous work, we have shown that an AlN seed layer can be used to promote oriented growth of Mo on Si and to prevent formation of silicides.^[15] Therefore, a similar approach was taken in this work. Although Au has a higher density than Mo, it was used as the top electrode in this work owing to the ease of fabrication.

There are many works discussing the properties of AlScN-based BAW resonators,^[9,16–23] but none have directly investigated the correlation between the crystal texture with acoustic resonator properties. Therefore, in this work, we have fabricated high overtone bulk acoustic wave resonators (HBAR) using stacks of AlScN/Mo/AlN on Si(111) with varying crystal texture to demonstrate its influence on the resonator properties, such as the effective electromechanical coupling coefficient (k_{eff}^2) and quality factor (Q) of the resonator. In our previous study, we observed that AlN exhibits epitaxy on Si(111).^[24] Therefore, to achieve epitaxy and to avoid a two-domain structure of AlN on Si(001) as shown by Lebedev et. al,^[25] we have used Si(111) substrates in this work. In addition, we also present a detailed explanation of the crystallographic orientation of Mo on AlN using X-ray diffraction (XRD) pole figures (PF).

2. Experimental Section

Evatec magnetron sputtering tools were used for depositing stacks of AlScN/Mo/AlN/Si. AlN and Mo layers were deposited in a planar configured module using an Evatec Clusterline 200II tool, followed by deposition of AlScN in a cosputtering module using an Evatec radiance tool. For AlN and Mo deposition, a 304 mm Al with a purity of 99.9995% and a Mo target with a purity of 99.95% were used. For AlScN deposition, 100 mm Al and Sc targets with a purity of 99.999% and 99.99% were used; the Sc concentration in the film was controlled by the power applied to these targets. An argon (Ar) based inductively coupled

Table 1. Growth parameters used for depositing $\text{Al}_{0.71}\text{Sc}_{0.29}\text{N}$ and Mo layers.

Layer	Temperature [°C]	Ar/N ₂ [sccm]	TSD [mm]
Mo	700	25/0	60
$\text{Al}_{0.71}\text{Sc}_{0.29}\text{N}$	700	0/20	65

Table 2. Thickness of the layers and scandium concentration in stacks 1 and 2 determined using TOF-SIMS.

Stack	Thickness [nm]					Sc Concentration [%]
	AlN	Mo	AlScN	Ti	Au	AlScN
1	111.6 ± 6.2	108.9 ± 6.7	293.4 ± 5.1	13.7 ± 1.7	111.2 ± 4.6	29
2	128.4 ± 5.3	110.5 ± 3.7	295.7 ± 6.8	14.3 ± 5.6	104.8 ± 0.4	29

plasma etching was used to clean the native oxide that was formed unintentionally when Si substrates were exposed to air. In our previous work, we have shown that growth temperature is a critical parameter to obtain epitaxial AlN on Si substrates.^[24] Therefore, the growth temperature of AlN seed layer was varied to produce $\text{Al}_{0.71}\text{Sc}_{0.29}\text{N}/\text{Mo}/\text{AlN}/\text{Si}$ stacks with different crystallographic textures, while keeping the growth parameters constant for the Mo and $\text{Al}_{0.71}\text{Sc}_{0.29}\text{N}$ layers. Growth parameters used for depositing Mo and $\text{Al}_{0.71}\text{Sc}_{0.29}\text{N}$ layers are listed in **Table 1**. The AlN seed layer was deposited at 50 °C and 70 °C, while keeping the Nitrogen (N₂) flow rate, power, and target substrate distance constant at 40 sccm, 5500 W, and 10 mm, respectively. The $\text{Al}_{0.71}\text{Sc}_{0.29}\text{N}/\text{Mo}/\text{AlN}/\text{Si}$ stack with AlN seed deposited at 50 °C will be called “stack 1”, while the $\text{Al}_{0.71}\text{Sc}_{0.29}\text{N}/\text{Mo}/\text{AlN}/\text{Si}$ stack with AlN seed deposited at 70 °C will be called “stack 2” in the next section of the article.

Ti/Au contacts with a theoretical resonator area of $70 \times 70 \mu\text{m}^2$ were evaporated on top of the $\text{Al}_{0.71}\text{Sc}_{0.29}\text{N}/\text{Mo}/\text{AlN}/\text{Si}$ stacks. For the thickness of these layers, see **Table 2**. The backside of the sample was polished in order to provide reflection of acoustic waves at the end of the substrate for a well-defined resonance cavity.

Crystal phase, mosaicity, and texture of the films were assessed through XRD using a PANalytical X'Pert Pro MRD diffractometer. An IONTOF M6 Plus time-of-flight secondary ion mass spectrometer (TOF-SIMS) with an integrated scanning probe microscope was used to determine the Sc concentration in the AlScN layer and the thickness of the layers. The frequency response of the stacks was measured using a PNA-X N5245A vector network analyzer. A PM300 Berlincourt piezometer was used to measure the longitudinal piezoelectric response.

3. Structural Properties

XRD- $2\theta/\theta$ scans recorded from “stack 1” and “stack 2” are depicted in **Figure 1(a)**. For both, reflections from $\text{Al}_{0.71}\text{Sc}_{0.29}\text{N}$ and AlN $000L$ ($l = 2, 4, 6$), Mo $hk0$ ($h = 1, 2$ and $k = 1, 2$), and Si hkl ($h = 1, 2, 3$; $k = 1, 2, 3$; and $l = 1, 2, 3$) were observed, proving that Mo grows with its (110) plane parallel to the (0001) basal plane of AlN on Si(111). Based on the $2\theta/\theta$ analysis, the orientational relationship (OR) of the stacks can be written as $\text{Al}_{0.71}\text{Sc}_{0.29}\text{N}(0001) \parallel \text{Mo}(110) \parallel \text{AlN}(0001) \parallel \text{Si}(111)$. Crystal phases that can be observed for Mo deposited on AlN depend on the polarity of AlN. When Mo is deposited on N-polar AlN, Mo is expected to grow with both (110) and (100) planes parallel to the AlN (0001) basal plane, while on metal-polar AlN, only Mo(110) plane is expected.^[26] In our previous work, we have shown that the AlN that we deposit is mixed-polar,^[24] which could be the reason for the absence of Mo 100 type reflections. Moreover, Mo 100 type

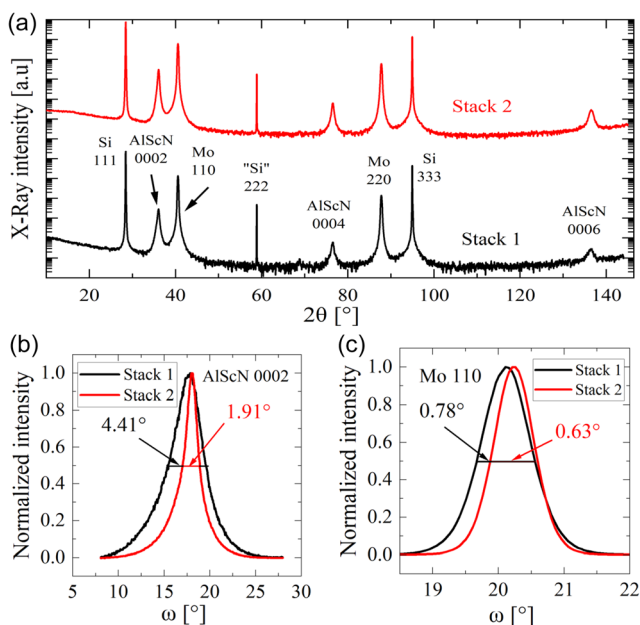


Figure 1. a) XRD- $2\theta/\theta$ analysis of stacks 1 and 2, and X-ray rocking curves measured from Stacks 1 and 2; b) $\text{Al}_{0.71}\text{Sc}_{0.29}\text{N}$ 0002 reflection; and c) Mo 110 reflection. Here, “Stack 1” and “Stack 2” correspond to fiber-textured and epitaxial Stacks of $\text{Al}_{0.71}\text{Sc}_{0.29}\text{N}/\text{Mo}/\text{AlN}/\text{Si}$, respectively.

reflections were observed when a similar stack was deposited on sapphire substrates.^[27] Figure 1(b) and (c) show XRD rocking curves of $\text{Al}_{0.71}\text{Sc}_{0.29}\text{N}$ 0002 and Mo 110 reflections, measured from stacks 1 and 2, respectively. The full width at half maximum

(FWHM) values were extracted by fitting a Pseudo-Voigt function to the respective rocking curves. The ω -FWHM of $\text{Al}_{0.71}\text{Sc}_{0.29}\text{N}$ 0002 reflection for stacks 1 and 2 was determined to be 4.41° and 1.91° , respectively, while the ω -FWHM of Mo 110 for stacks 1 and 2 was determined to be 0.78° and 0.63° , respectively. The ω -FWHM values indicate that the crystalline quality of both $\text{Al}_{0.71}\text{Sc}_{0.29}\text{N}$ and Mo improve when deposited on AlN seed grown at 70°C . The improvement in the crystal quality of Mo may also be partly attributed to the increased thickness of the AlN seed layer when grown at 70°C (see Table 2).

XRD-PF recorded at a 2θ angle of 37.9° from stacks 1 and 2 is shown in Figure 2(a) and (c), respectively. XRD-PF obtained from stack 1 revealed a ring-like structure at $\chi \approx 60^\circ$, indicating that AlScN is fiber-textured. In our previous work, we have shown that Mo grown on fiber-textured AlN is fiber-textured, while on epitaxial AlN it has a three-domain structure.^[15] Due to the fiber-textured nature of Mo on fiber-textured AlN, AlScN grains also grow in a fiber-textured manner, resulting in a ring-like feature as seen in Figure 2(a). Interestingly, for stack 2, there appears to be a sixfold symmetry with two maxima at $\chi \approx 60^\circ$. At a 2θ angle of 40° , four reflections of Mo are allowed, since this angle is close to the 2θ angle at which the XRD-PF was measured, it is possible that these reflections are from Mo. Since Mo has a three-domain structure on epitaxial AlN, the additional two domains contribute to eight more reflections, resulting in the 12 peaks as seen in Figure 2(b). The broad reflection observed between the two pairs of reflections corresponds to $\text{Al}_{0.71}\text{Sc}_{0.29}\text{N}$. Since the $\text{Al}_{0.71}\text{Sc}_{0.29}\text{N}$ reflection is broadened, a distinct OR with Mo could not be determined. Although the epitaxial relationship is unclear, from Figure 2(a) and (b), one could argue that the allowed degree of rotation for the $\text{Al}_{0.71}\text{Sc}_{0.29}\text{N}$ grains along

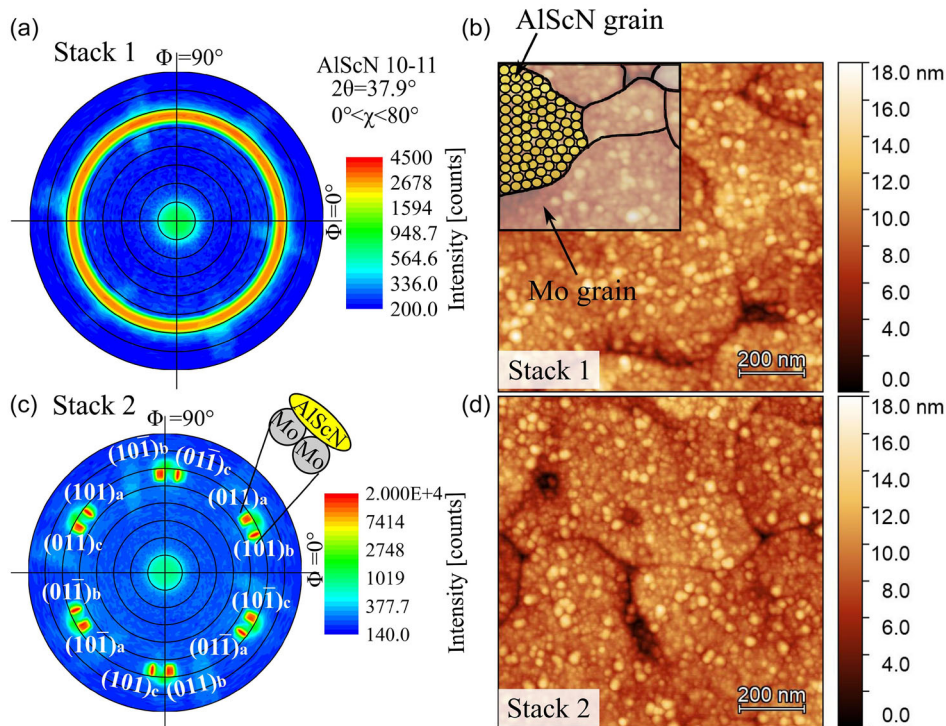


Figure 2. XRD-PF of a) stack 1 and c) stack 2 recorded at a 2θ angle of 37.9° , covering χ angles from 0° to 80° ; AFM images of b) stack 1 and d) stack 2.

the *c*-axis is limited in stack 2 when compared to stack 1. Figure 2(b) and (d) show atomic force microscopy (AFM) images from stacks 1 and 2, respectively. The large grain seen in the images corresponds to Mo, while the smaller grains correspond to AlScN grains, as depicted in Figure 2(b). AlScN in both the stacks showed a similar roughness of ≈ 1.9 nm.

4. Fabrication of high overtone bulk acoustic wave resonators (HBARs)

In order to fabricate HBAR, ≈ 20 nm Ti/ ≈ 100 nm Au electrodes were evaporated on stacks 1 and 2. To grind and polish the back side of the wafer, the wafers were bonded to a dummy substrate, followed by grinding and polishing of the backside of the substrate. After polishing the backside of the wafer, the wafers were debonded from the dummy substrate. A schematic of the fabrication route is shown in Figure 3. Since the layers in stacks 1 and 2 were determined to be fiber textured and epitaxial, respectively, the resonators fabricated using stacks 1 and 2 will be called “fiber-HBAR” and “epi-HBAR,” respectively. The resonator topology of fiber-HBAR and epi-HBAR, from which the electrical measurements reported in the following section are shown in Figure S2(a) and (b), respectively, in Supplementary file. From the images, it can be seen that the resonator area for both fiber-HBAR and epi-HBAR was approximately the same.

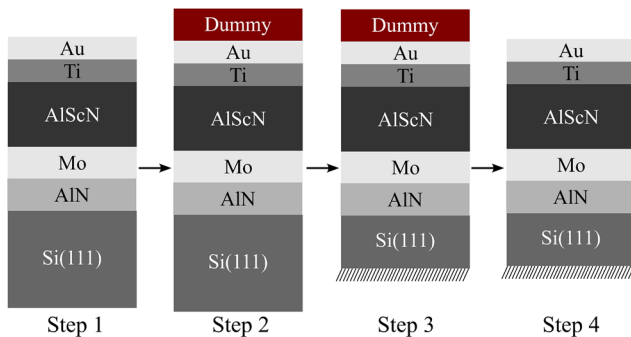


Figure 3. Fabrication route employed to realize an HBAR resonator.

Thickness of the layers and the Sc concentration in AlScN of stacks 1 and 2 were determined using TOF-SIMS and are listed in Table 2. The table demonstrates that both stacks have similar layer thickness and Sc concentration in the AlScN layer.

5. Resonator Properties of EPI and Fiber-HBAR

The input impedance (Z_{in}) of epi-HBAR and fiber-HBAR is illustrated in Figure 4(a). The fundamental resonance frequency, i.e., resonance frequency of the piezoelectric film for both the HBARs occurs at ≈ 4 GHz. The shift observed in the resonant modes, as depicted in the inset of Figure 4(a), could be attributed to a slight variation in thickness of the substrate after grinding and polishing processes. This thickness variation in the substrate is also reflected as a shift in the spacing between the parallel resonant frequencies (SPRF), as depicted in Figure 4(b). The SPRF is inversely proportional to the length of the resonance cavity d , i.e., the thickness of the substrate.^[28,29] For information on the SPRF, the readers are directed to literature.^[30] Specifically, the SPRF of epi-HBAR is higher than fiber-HBAR, indicating that the substrate thickness of epi-HBAR is less than that of fiber-HBAR. Moreover, the substrate thickness (t_{sb}) of epi-HBAR and fiber-HBAR was found to be ≈ 120 and ≈ 124 μ m, respectively.

For both epi-HBAR and fiber-HBAR, a noticeable trend is the decrease in resonance amplitude as the spectral distance from the fundamental frequency increases. The fundamental frequency is primarily modulated by the piezoelectric layer, and as the distance from the fundamental frequency increases, the influence of the substrate becomes more prominent, resulting in reduction of the resonance amplitude.

The effective electromechanical coupling coefficient (k_{eff}^2),^[31] for each mode in the resonance spectrum was calculated using

$$k_{eff}^2 = \frac{\pi^2 f_s f_p - f_s}{4 f_p f_p} \quad (1)$$

where f_s and f_p are series and parallel resonance frequencies, respectively. f_s and f_p , as defined by the IEEE standards, were identified from the real part of Z_{in} and admittance Y_{in} .^[32] k_{eff}^2 for epi and fiber-HBAR, was calculated using Equation (1)

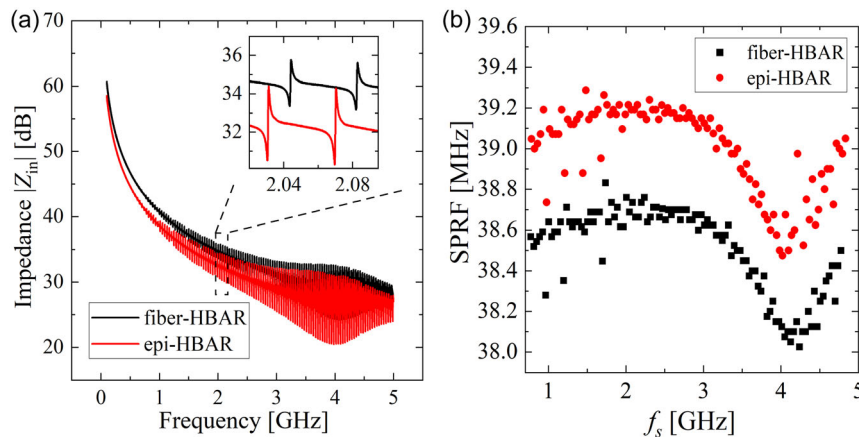


Figure 4. a) Impedance characteristics $|Z_{in}|$ and b) spacing between parallel resonant frequencies of a fiber-HBAR and epi-HBAR.

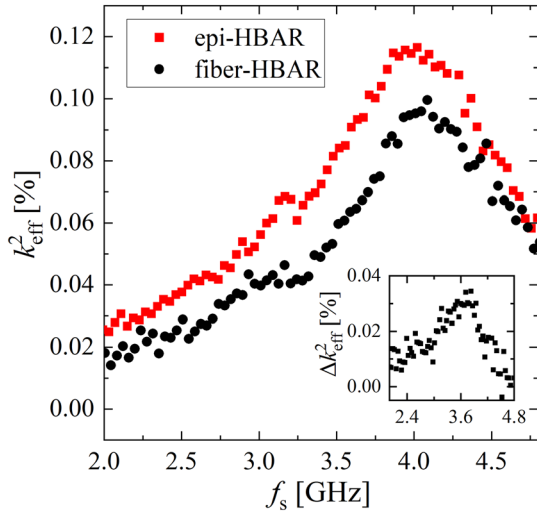


Figure 5. Effective electromechanical coupling coefficient (k_{eff}^2) calculated from the resonant spectrum of a fiber-HBAR and epi-HBAR.

and is plotted against the corresponding series resonant frequency (f_s) in **Figure 5**.

Figure 5 shows that for both fiber-HBAR and epi-HBAR, the k_{eff}^2 reaches a maximum at ≈ 4 GHz, and it reduces as the distance from the fundamental resonance increases. The reason for the maximum is due to the fact that the fundamental frequency is predominantly modulated by the piezoelectric film. It can also be observed that the k_{eff}^2 of an epi-HBAR is higher than fiber-HBAR. The difference in k_{eff}^2 of an epi and fiber-HBAR (Δk_{eff}^2), which is shown as an inset in Figure 5, reached a maximum of $\approx 0.03\%$ at ≈ 4 GHz. Additionally, the average SPRF ($\overline{\text{SPRF}}$) and average k_{eff}^2 ($\overline{k_{\text{eff}}^2}$), calculated from the SPRF and k_{eff}^2 spectra are listed in **Table 3**.

As discussed previously, the thickness of epi-HBAR is slightly lower than that of fiber-HBAR, which is expected to improve its k_{eff}^2 .^[33] To investigate whether this difference could have accounted for the observed increase in k_{eff}^2 , an epi-HBAR with a substrate thickness of $\approx 110 \mu\text{m}$ (“Thin” epi-HBAR) was fabricated. SPRF was employed to indirectly assess the change in substrate thickness. The outcomes of the results are summarized in **Table 3**. Reducing the substrate thickness of an epi-HBAR increased the $\overline{\text{SPRF}}$ by ≈ 3.8 MHz, while the $\overline{k_{\text{eff}}^2}$ increased by $\approx 0.017\%$. When comparing this observation with $\overline{\text{SPRF}}$ and $\overline{k_{\text{eff}}^2}$ of epi and fiber-HBAR, which were ≈ 0.49 MHz and $\approx 0.013\%$,

Table 3. Average SPRF, average effective electromechanical coupling coefficients, and substrate thickness of the HBAR studied in this work.

Resonator	Substrate thickness (t_{sb}) [μm]	Average SPRF ($\overline{\text{SPRF}}$) [MHz]	Average k_{eff}^2 ($\overline{k_{\text{eff}}^2}$) [%]
epi-HBAR	≈ 120	38.99	0.054
fiber-HBAR	≈ 124	38.51	0.041
“thin” epi-HBAR	≈ 110	42.7	0.071

respectively, it becomes evident that the change in substrate thickness has a negligible contribution to the increase in k_{eff}^2 depicted in **Figure 5**. The average SPRF and average k_{eff}^2 listed in **Table 3** were calculated from the plots shown in **Figure S1(a)** and **(b)** (see Supplementary file).

In **Section III**, it was shown that the ω -FWHM of the AlScN 0002 reflection for the produced epitaxial AlScN to be better than the produced fiber-textured AlScN. The rocking curve width, which is an indication of the degree of c -axis orientation of the AlScN grains, is expected to have a direct impact on d_{33} ,^[34] and hence could be the reason for the observed improvement in k_{eff}^2 (see **Figure 5**).^[12] In order to quantify the change in longitudinal piezoelectric response, fiber texture and epitaxial stacks of $\text{Al}_{0.71}\text{Sc}_{0.29}\text{N}/\text{AlN}/\text{Si}$ were prepared and analyzed using Berlincourt piezometer. The longitudinal piezoelectric response of the fiber textured and epitaxial AlScN was found to be $(-8.82 \pm 0.05) \text{ pC N}^{-1}$ and $(-9.14 \pm 0.05) \text{ pC N}^{-1}$. Additionally, variations in number of abnormally oriented grains (AOG) can also influence the longitudinal piezoelectric response.^[35] AFM images ($5 \times 5 \mu\text{m}^2$) of stack 1 and stack 2 (see **Figure S3** in Supplementary file) revealed that the produced “epi-AlScN” is rougher than “fiber-AlScN”, but both the stacks exhibit a similar number of AOG. This indicates that the observed improvement in longitudinal piezoelectric response is not attributed to AOG. A longitudinal piezoelectric response of 16 pC N^{-1} has been reported for $\text{Al}_{0.71}\text{Sc}_{0.29}\text{N}$,^[8] which is significantly higher than the longitudinal piezoelectric response values obtained for both fiber-textured and epitaxial $\text{Al}_{0.71}\text{Sc}_{0.29}\text{N}$ in this work. Factors such as presence of an AlN seed layer,^[36] thickness of the $\text{Al}_{0.71}\text{Sc}_{0.29}\text{N}$ layer,^[34] presence of AOG,^[35] or inversion domain boundaries could have caused the observed reduction in longitudinal piezoelectric response. Nevertheless, the outcome of the piezometer measurements clearly shows that the longitudinal piezoelectric response of epitaxial $\text{Al}_{0.71}\text{Sc}_{0.29}\text{N}$ is larger than that of fiber-textured $\text{Al}_{0.71}\text{Sc}_{0.29}\text{N}$, supporting the results observed in **Figure 5**.

The Bode Q (Q_{bode}) can be determined using Equation 2.^[37] ϕ and $\text{mag}(S_{11})$ in the equation are the phase and magnitude of the measured scatter parameters (S_{11}). In order to validate Q_{bode} calculations, $Q_{\text{Dicke-Z}}$, and $Q_{\text{Dicke-Y}}$ were calculated using Equation 3 and 4, respectively.^[38] R and X in Equation 3 were calculated from impedance Z as $Z = R + jX$, while G and B in Equation 4 were calculated from admittance Y as $Y = G + jB$.

$$Q_{\text{bode}} = \omega \frac{d\phi}{d\omega} \frac{\text{mag}(S_{11})}{1 - (\text{mag}(S_{11}))^2} \quad (2)$$

$$Q_{\text{Dicke-Z}} = \frac{\omega}{2R} \frac{\partial X}{\partial \omega} \quad (3)$$

$$Q_{\text{Dicke-Y}} = \frac{\omega}{2G} \frac{\partial B}{\partial \omega} \quad (4)$$

Q_{bode} determined for fiber-HBAR and epi-HBAR at ≈ 4 GHz shown in **Figure 6(a)**, reveals that the Q_{bode} of “normal modes” and spurious modes is higher for epi-HBAR. Q_{bode} , $Q_{\text{Dicke-Z}}$, and $Q_{\text{Dicke-Y}}$ of “normal modes” and spurious modes determined for a larger frequency range also showed a similar trend

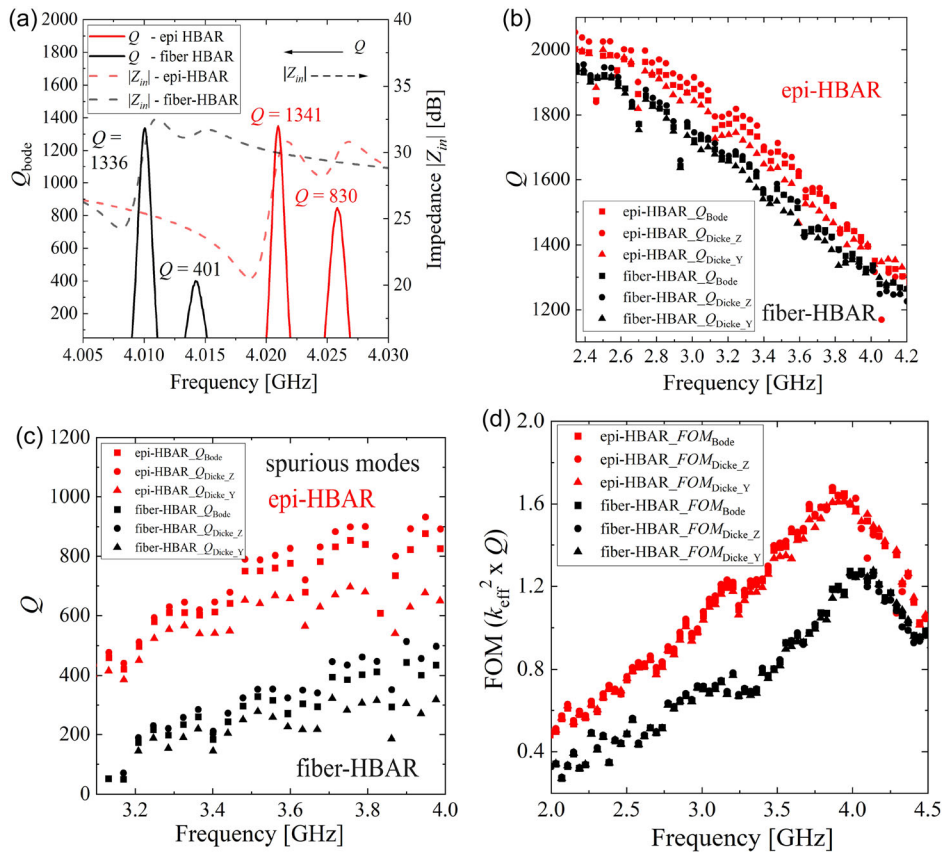


Figure 6. Quality factor Q_{bode} of a fiber and epi-HBAR extracted a) at ≈ 4 GHz, b) for “normal modes” in the frequency range ≈ 2 and 4.2 GHz, c) for spurious modes in the frequency range ≈ 3 and 4.2 GHz, and d) FOM ($Q_{\text{bode}} \times k_{\text{eff}}^2$) calculated for “normal modes” in the frequency range ≈ 2 and 4.5 GHz.

(see Figure 6(b) and (c)). In our previous work, we have shown that the electrical resistivity of epitaxial Mo is lower than fiber-textured Mo due to presence of high symmetry grain boundaries.^[15] Electrical resistivity introduces Ohmic losses in the resonator, reducing its Q .^[39] The improved resistivity of epitaxial Mo could be the reason for the observed improvement in Q . The figure of merit (FOM) [$Q \times k_{\text{eff}}^2$] calculated by using Q_{bode} , Q_{Dicke_Z} , Q_{Dicke_Y} , and k_{eff}^2 for the “normal modes” of both epi-HBAR and fiber-HBAR are shown in Figure 6(d). The figure clearly demonstrates that the performance of epi-HBAR is better than fiber-HBAR. FOM at ≈ 4 GHz for epi-HBAR and fiber-HBAR was determined to be 1.57 and 1.25, respectively, which is $\approx 25\%$ improvement in resonator performance with epitaxial piezoelectric and electrode material. The results indicate a significant gain in performance of the resonator by employing epitaxial layers of Mo and AlScN. Therefore, epitaxial Mo and AlScN emerge as a superior candidate for BAW devices when compared to their fiber-textured equivalents.

6. Conclusion

In this study, we systematically studied the effect of texture on the structural properties and performance of HBAR

fabricated using the stack Au-Ti/AlScN/Mo/AlN/Si. The texture of Mo and AlScN was controlled by changing the deposition conditions of AlN seed layer while keeping all the other parameters constant. TOF-SIMS and XRD results confirm that the only difference between the two stacks is the crystalline quality. Our results indicate that the improvement in crystalline quality of both epitaxial Mo and AlScN leads to a significant improvement in their resonator properties. HBAR fabricated demonstrate that the resonator that employs epitaxial AlScN has a superior k_{eff}^2 than fiber-textured material. Reasons for this improvement are attributed to the improved crystal quality, which leads to improvement of the longitudinal piezoelectric response for epitaxial AlScN. In addition, epi-HBAR has a higher Q factor than fiber-HBAR. The improvement in Q could be due to a combination of reduced losses at grain boundaries or due to reduced resistivity of the electrodes. In conclusion, the study revealed that epitaxial growth of AlScN on Mo and AlN substrates resulted in better structural properties and enhanced performance of the HBAR compared to the fiber-textured stack. These findings have implications for the development of BAW devices, where devices with higher Q factor and k_{eff}^2 are required. Further improvements in the resonator properties are planned by having epitaxial Mo as a top electrode.

Supporting Information

Supporting Information is available from the Wiley Online Library or from the author.

Acknowledgements

This project was performed within the framework of COMET - Competence Centers for Excellent Technologies and ASSIC Austrian Smart Systems Integration Research Center, which is funded by BMVIT, BMDW, and the Austrian provinces of Carinthia and Styria. The COMET program is run by FFG. The authors would also like to thank Nadine Brückner for performing XRD measurements, Rafael Silberer, Stefan Rombach, and Ulrike Meinold for grinding and polishing the silicon substrates, and Dr. Vadim Lebedev for fruitful discussions.

Open Access funding enabled and organized by Projekt DEAL.

Conflict of Interest

The authors declare no conflict of interest.

Data Availability Statement

The data that support the findings of this study are available from the corresponding author upon reasonable request.

Keywords

aluminum nitride, AlScN, bulk acoustic wave, epitaxy, high overtone bulk acoustic wave resonators, magnetron sputtering, molybdenum

Received: February 28, 2025

Revised: July 8, 2025

Published online:

- [1] R. Aigner, G. Fattinger, M. Schaefer, K. Karnati, R. Rothmund, F. Dumont, *2018 IEEE International Electron Devices Meeting (IEDM)*, IEEE, **2018**, pp. 14–5.
- [2] T. Nishihara, T. Yokoyama, T. Miyashita, Y. Satoh, *2002 IEEE Ultrasonics Symp., 2002 Proc.*, Vol. 1, IEEE, **2002**, pp. 969–972.
- [3] S. Mahon, *IEEE Trans. Semicond. Manuf.* **2017**, *30*, 494.
- [4] R. Aigner, *2008 IEEE Ultrasonics Symp.*, IEEE, **2008**, pp. 582–589.
- [5] D. Malocha, in *2010 IEEE 11th Annual Wireless and Microwave Technology Conf. (WAMICON)*, IEEE, **2010**, pp. 1–7.
- [6] R. S. Naik, J. J. Lutsky, R. Reif, C. G. Sodini, A. Becker, L. Fetter, H. Huggins, R. Miller, J. Pastalan, G. Rittenhouse, Y.-H. Wong, *IEEE Trans. Ultrason., Ferroelectrics, Frequency Control* **2000**, *47*, 292.
- [7] K. Tonisch, V. Cimalla, C. Foerster, H. Romanus, O. Ambacher, D. Dontsov, *Sensors Actuators A: Phys.* **2006**, *132*, 658.
- [8] M. Akiyama, T. Kamohara, K. Kano, A. Teshigahara, Y. Takeuchi, N. Kawahara, *Adv. Mater.* **2009**, *21*, 593.
- [9] G. Wingqvist, F. Tasnadi, A. Zukauskaitė, J. Birch, H. Arwin, L. Hultman, *Appl. Phys. Lett.* **2010**, *97*.
- [10] J. B. Shealy, J. B. Shealy, P. Patel, M. D. Hodge, R. Vetry, J. R. Shealy, in *2016 IEEE Radio and Wireless Symp. (RWS)*, IEEE, **2016**, pp. 16–19.
- [11] R. Vetry, M. D. Hodge, J. B. Shealy, in *2018 IEEE Inter. Ultrasonics Symp. (IUS)*, IEEE, **2018**, pp. 206–212.
- [12] H. Loebel, M. Klee, C. Metzmacher, W. Brand, R. Milsom, P. Lok, *Mater. Chem. Phys.* **2003**, *79*, 143.
- [13] M. Ueda, T. Nishihara, S. Taniguchi, T. Yokoyama, J. Tsutsumi, M. Iwaki, Y. Satoh, *Jpn. J. Appl. Phys.* **2007**, *46*, 4642.
- [14] S.-H. Lee, K. H. Yoon, J.-K. Lee, *J. Appl. Phys.* **2002**, *92*, 4062.
- [15] B. Sundarapandian, M. Raghuvanshi, P. Straňák, Y. Yu, H. Lyu, M. Prescher, L. Kirste, O. Ambacher, *Appl. Phys. Lett.* **2025**, *126*.
- [16] K. Umeda, H. Kawai, A. Honda, M. Akiyama, T. Kato, T. Fukura, in *2013 IEEE 26th Inter. Conf. on Micro Electro Mechanical Systems (MEMS)*, IEEE, **2013**, pp. 733–736.
- [17] Z. Hao, M. Park, D. G. Kim, A. Clark, R. Dargis, H. Zhu, A. Ansari, in *2019 IEEE MTT-S Inter. Microwave Symp. (IMS)*, IEEE, **2019**, pp. 786–789.
- [18] C. Masamune, T. Yanagitani, *AIP Adv.* **2021**, *11*.
- [19] C.-Y. Chung, Y.-C. Chen, Y.-C. Chen, K.-S. Kao, Y.-C. Chang, *Coatings* **2021**, *11*, 1151.
- [20] T. Yanagitani, K. Arakawa, K. Kano, A. Teshigahara, M. Akiyama, *2010 IEEE Inter. Ultrasonics Symp.*, IEEE, **2010**, pp. 2095–2098.
- [21] R. Matloub, A. Artieda, C. Sandu, E. Milyutin, P. Mural, *Appl. Phys. Lett.* **2011**, *99*.
- [22] M. Moreira, J. Bjurström, I. Katardjev, V. Yantchev, *Vacuum* **2011**, *86*, 23.
- [23] T. Yanagitani, M. Suzuki, *Appl. Phys. Lett.* **2014**, *105*.
- [24] B. Sundarapandian, A. Yassine, L. Kirste, M. Baeumler, P. Straňák, E. Fisslthaler, M. Prescher, M. Yassine, A. Nair, M. Raghuvanshi, O. Ambacher, *J. Appl. Phys.* **2023**, *134*.
- [25] V. Lebedev, J. Jinschek, U. Kaiser, B. Schröter, W. Richter, J. Kräußlich, *Appl. Phys. Lett.* **2000**, *76*, 2029.
- [26] C. Gao, O. Brandt, S. C. Erwin, J. Lähnemann, U. Jahn, B. Jenichen, H.-P. Schönherr, *Physi. Rev. B—Condens. Matter Mater. Phys.* **2010**, *82*, 125415.
- [27] N. Wolff, S. Fichtner, B. Haas, M. R. Islam, F. Niekil, M. Kessel, O. Ambacher, C. Koch, B. Wagner, F. Lofink, et al., *J. Appl. Phys.* **2021**, *129*.
- [28] J. Rosenbaum, *Bulk acoustic wave theory and devices*, Artech House on Demand, **1988**.
- [29] D. Rabus, J. Friedt, S. Ballandras, T. Baron, É. Lebrasseur, É. Carry, *J. Appl. Phys.* **2015**, *118*.
- [30] Y. Zhang, Z. Wang, J. D. N. Cheeke, *IEEE Trans. Ultrason., Ferroelectrics, Frequency Control* **2003**, *50*, 321.
- [31] Q. Chen, Q.-M. Wang, *Appl. Phys. Lett.* **2005**, *86*.
- [32] “IEEE standard on piezoelectricity,” ANSI/IEEE Std 176-1987, 1988.
- [33] T. Baron, E. Lebrasseur, F. Bassignot, G. Martin, V. P’etrini, S. Ballandras, *Modeling and Measurement Methods for Acoustic Waves and for Acoustic Microdevices*, **2013**, 297.
- [34] J. Martin, P. Mural, M.-A. Dubois, A. Pezous, *J. Vac. Sci. Technol. A: Vac., Surfaces, Films* **2004**, *22*, 361.
- [35] Y. Lu, M. Reusch, N. Kurz, A. Ding, T. Christoph, L. Kirste, V. Lebedev, A. Žukauskaitė, *Phys. Status Solidi A* **2018**, *215*, 1700559.
- [36] J. Su, S. Fichtner, M. Z. Ghori, N. Wolff, M. R. Islam, A. Lotnyk, D. Kaden, F. Niekil, L. Kienle, B. Wagner, F. Lofink, *Micromachines* **2022**, *13*, 783.
- [37] D. A. Feld, R. Parker, R. Ruby, P. Bradley, S. Dong, in *2008 IEEE Ultrasonics Symp.*, IEEE, **2008**, pp. 431–436.
- [38] C. G. Montgomery, R. H. Dicke, E. M. Purcell, *Principles Of Microwave Circuits*, IET **1987**, p. 25.
- [39] R. Thalhammer, G. Fattinger, M. Handtmann, S. Marksteiner, in *2006 IEEE MTT-S Inter. Microwave Symp. Digest*, IEEE, **2006**, pp. 390–393.